In situ growth, structure, and real-time chemical reactivity of well-defined CeO$_x$-Ru(0001) model surfaces

David C. Grinter [a], Sanjaya D. Senanayake [a,*], Jan Ingo Flege [b,*]

[a] *Chemistry Department, Brookhaven National Laboratory, Upton, NY, USA*
[b] *Institute of Solid State Physics, University of Bremen, Bremen, Germany*

ARTICLE INFO

ABSTRACT

Ceria is an important material for chemical conversion processes in catalysis. Its intrinsic properties as a reducible oxide can be exploited to achieve catalytic selectivity and activity. However, numerous phenomenological characteristics of ceria remain unknown and its active nature is ever slowly being unraveled. Well defined models of ceria (111) are an important way to systematically study these properties and take advantage of new in situ methods that require pristine materials that allow for the interrogation of the most fundamental traits of this material. The ceria-Ru(0001) model is now the most well studied model surface with numerous aspects of its preparation, atomic structure and reactivity studied by several groups. The preparation of CeO$_x$ structures oriented with a (111) surface termination can be achieved through molecular beam deposition, facilitating the growth of well-defined nanostructures, microparticles, and films on the Ru(0001) surface. The growth mechanism exploits the epitaxial relationship between CeO$_x$ and Ru to form a carpet mode of well oriented layers of O—Ce—O. These models can be studied to unravel the atomic structure and the oxidation state (Ce^{4+} and Ce^{3+}), as prepared and under redox conditions (reduction/oxidation) or with reaction using reactants (*e.g.*, H$_2$, methanol). Here, we present a discussion of these most recent observations pertaining to the growth mode, arrangement of atoms on the surface, characteristic chemical state, and redox chemistry of the CeO$_x$-Ru surface. With insights from these studies we propose new strategies to further unravel the chemistry of ceria.

© 2016 Elsevier B.V. All rights reserved.

1. Introduction

The utility of cerium oxide as a remarkable heterogeneous base catalyst material is now fully realized, with ample evidence in the literature for its versatile use in numerous chemical conversion processes including the water-gas shift (WGS) reaction [1,2], CO oxidation [3], CO PROX [4], de-NOx (automotive exhausts) [5], CO$_2$ hydrogenation [6], olefin hydrogenation [7], methane activation [8], alcohol steam reforming [9], and others [10]. In all cases, the intrinsic phenomenological properties of ceria allow reactions to be steered (*selectivity*), stabilized, and performance enhanced (*activity*). Our understanding of how such active traits manifest their role in reactions is ever evolving, enriched with the development of new analytical tools for *in situ* analysis. We are now entering a phase of research and development where we are starting to learn about the dynamic nature of the properties of ceria that prevail under reaction conditions and how we can exploit them to achieve greater improvements in catalytic chemistry.

The primary catalytic use of ceria is as a reducible oxide support, where it has been commonly used as a substrate to anchor, activate, and promote metals or other oxides. However, the primitive perception that this oxide (and others) is an inert support and unlikely to activate reactions has evolved to affirm important support effects, including atomic and defect geometry [11], electronic [12] and ligand effects [13,14] that were not realized before. Furthermore, the oxides used as nano-catalysts [15] or as mixed oxides [16,17] have allowed their exploitation as the active agent in several reactions. The key factors that make ceria important remain its facile reducibility, high oxygen storage capacity (OSC), simply interchangeable oxidation states (Ce^{4+}, Ce^{3+}), electron rich centers (4f) and stable crystal structure. The fundamental investigations into the atomic structure, physical and chemical properties, surface chemistry, and electronic structure of ceria have allowed for a more complete understanding of challenging observations made at reaction conditions.

To date, a large body of work has been devoted to well-defined cerium oxide surfaces supported on a variety of metal sub-
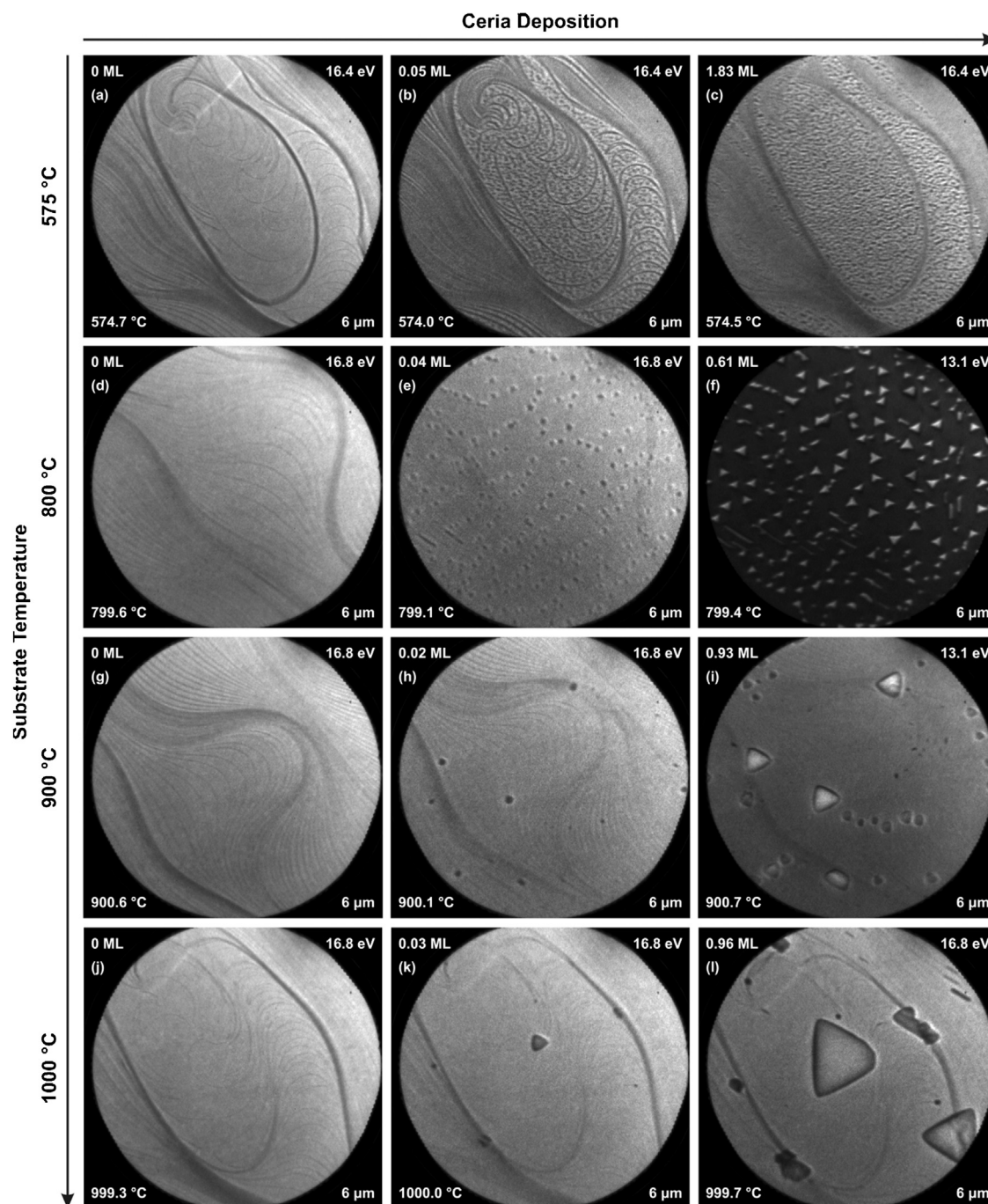
Ceria Deposition

Fig. 1. Growth of ceria on Ru(0001) at different substrate temperatures and stages of growth (increasing deposited amount of ceria). From left to right: advancing stage of growth. From top to bottom: increasing substrate temperature. The ceria island size increases with substrate temperature while the ceria island density decreases. The different contrast in panels (f) and (i) compared to the other panels is due to a different electron kinetic energy. The cerium deposition rate is the same in all cases. Reprinted with permission from Ref. [26]. Copyright 2013 American Chemical Society.

strates, of which the $CeO_x(111)$-Ru(0001) model has been devoted considerable attention. This system, initially prepared as a continuous CeO_x film [18–20], has facilitated experimental investigations of the atomic structure (scanning tunneling microscopy (STM)), chemical state (X-ray photoelectron spectroscopy (XPS)), and surface chemistry upon reaction with numerous reactants [21–24]. In addition, we now have recipes to synthesize well defined $CeO_x(111)$ nanostructures and micron-sized particles [25–27] as well as surfaces with careful control of cation densities (Ce^{4+}/Ce^{3+}) and Ce/O stoichiometry on Ru(0001) [28]. This has greatly expanded the use of this particular system to further interrogate fundamental cat-

alytic properties [20,29,30], *e.g.*, as a well-defined oxide support for post-grown metallic nanoparticles [31–34]. We have exploited this particularly to study the dynamic properties of ceria by using new *in situ* methods such as Low Energy Electron Microscopy (LEEM) and X-ray Photoemission Electron Microscopy (XPEEM).

In this perspective article, we provide a coherent overview of the versatile CeO_x-Ru(0001) system by covering essential aspects of the prevailing preparation methodology, the typical growth mechanism, atomic surface structure and its chemical state after preparation. In doing so, we also highlight the importance of the catalyst surface structure to effect the chemical reactivity of ceria
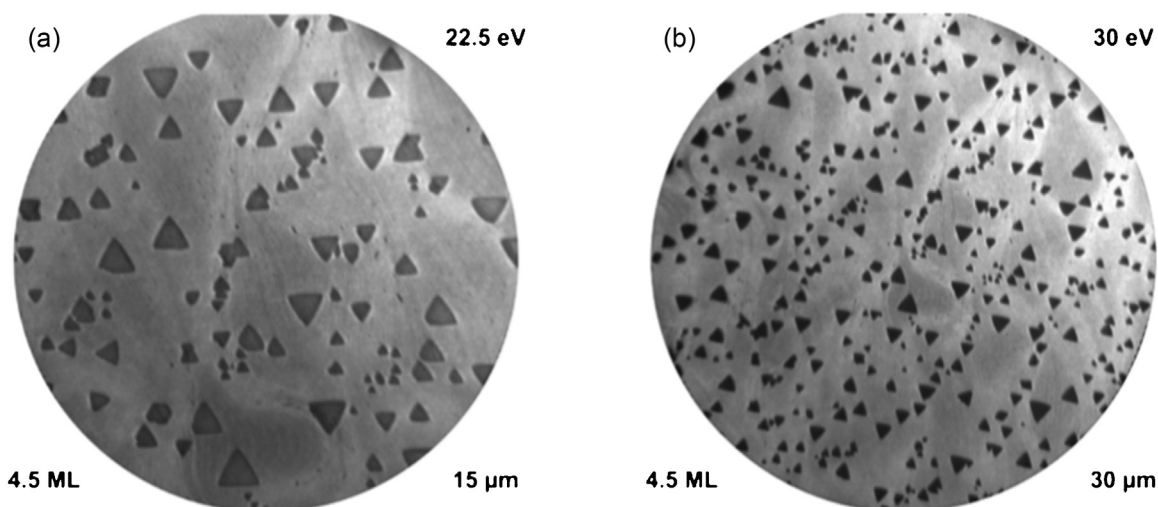
Fig. 2. Different fields of view of ceria grown on Ru(0001) at a 900 °C substrate temperature and an oxygen partial pressure of 5×10^{-7} Torr showing the nucleation behavior of the islands on substrate terraces and step bunches. (a) FOV = 15 μm and (b) FOV = 30 μm. Ceria islands with an almost perfect triangular shape preferentially develop on substrate terraces while the island density is strongly increased at step bunches. Reprinted with permission from Ref. [26]. Copyright 2013 American Chemical Society.
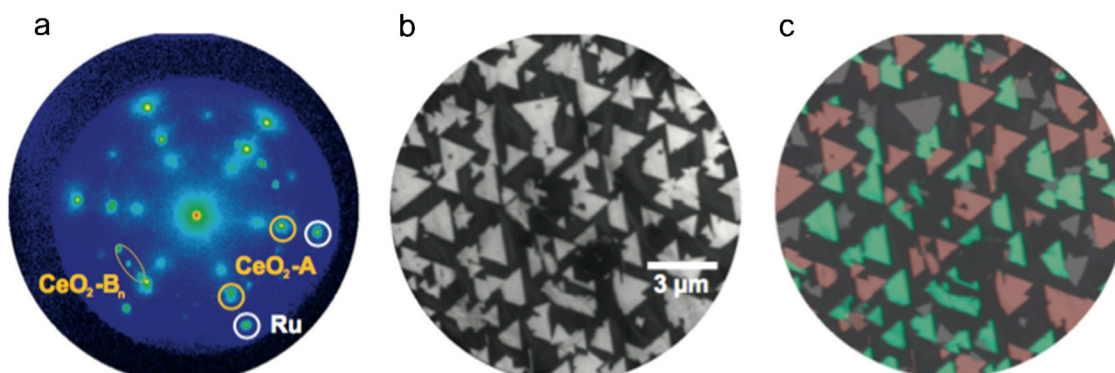

Fig. 3. (a) Low-energy electron diffraction pattern acquired after cerium oxide growth (E = 40 eV). The integer reflections of Ru(0001), CeO$_2$(111)-A, and CeO$_2$(111)-B are labeled. (b) Bright-field (BF) LEEM image, and (c) composite image consisting of one BF image (displayed in (b)) and two dark-field LEEM images recorded using the (10) reflections of A/A'-type cerium oxide as indicated in (a). The gray domains of the BF image that do not coincide with cerium oxide islands in the DF images highlight the azimuthally rotated B$_n$-type cerium oxide domains. Reprinted from Ref. [25], with permission from Elsevier.

in redox reactions. Finally, we discuss the prospects of applying real time *in situ* methods (LEEM/XPEEM) for probing chemical reactivity in ceria based model catalysts.

2. Growth of CeO$_x$ on Ru(0001)

Low Energy Electron Microscopy (LEEM) is particularly well suited to study the growth of CeO$_x$ on Ru(0001) surfaces, due to its high resolution, large temperature range, and rapid image acquisition rate [35]. As a full-field diffractive imaging technique with full ultrahigh-vacuum compatibility [36,37], *real-time* monitoring of surface processes may readily be performed both in real and reciprocal space, effectively spanning the whole range from the atomic scale (*via* diffraction mode) to the nanometer and micrometer scale. Furthermore, with an improved understanding of the process of contrast formation in the microscope [38–41] a quantitative *in situ* assessment of surface structure as well as thermodynamically and kinetically driven surface phenomena is viable; moreover, the increasing availability of LEEM instruments equipped with energy filters at synchrotron radiation sources offers the attractive prospect of complementary characterization by spatially-resolved X-ray absorption spectroscopy (XAS) and Photoemission Electron Microscopy (XPEEM) [42] techniques. Three-dimensional information on crystallographic structure and molecular adsorption sites

may be obtained by analyzing the dependence of the local electron reflectivity on electron kinetic energy, the so-called intensity-voltage ($I(V)$) curve [43]. This approach currently provides the highest spatial resolution and may be expected to become even more powerful with the advent of aberration-corrected microscopes [44] that have pushed the achievable lateral resolution down to less than 2 nm. In the following, we provide a comprehensive overview of the novel insights into the ceria-ruthenium system that have been obtained in previous studies by applying this combined LEEM/PEEM technique.

LEEM images (see the supplemental material for a real-time growth movie) were recorded by Kaemena et al. [26] for the growth of ceria on Ru(0001) as the amount of deposited ceria increased and at different substrate temperatures as displayed in Fig. 1: (575 °C, (a)–(c); 800 °C, (d)–(f); 900 °C, (g)–(i); 1000 °C, (j)–(l)). Initially only the Ru(0001) atomic steps (thin dark lines) and step bunches (broad dark lines) appear, with atomically flat terraces. Nucleation commences visibly at low coverages of 0.02–0.05 ML (second series), and higher coverages 0.61 and 1.83 ML (third series).

At 575 °C very small ceria islands nucleate at high density, and continued growth results in the formation of a closed ceria film. With increased temperature, the island size increases while the island density decreases; also, with increased temperature the islands adopt an almost perfect triangular shape. The nucle-
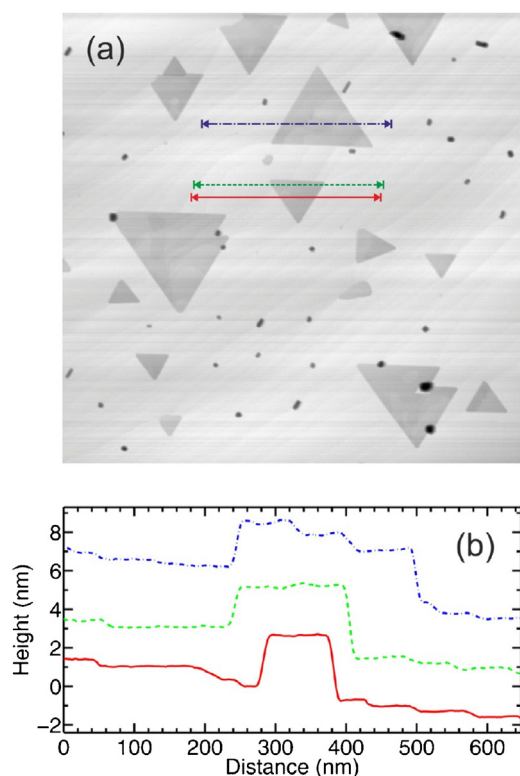
Fig. 4. (a) $1.5 \times 1.5\ \mu m^2$ *ex situ* AFM image of fully oxidized ceria islands on Ru(0001) with a coverage of 1 ML grown at a substrate temperature of 800 °C and an oxygen partial pressure of 5×10^{-7} Torr. (b) Respective line scans showing approximately 3 nm tall ceria islands with sharp edges and the terraces and steps of the Ru(0001) substrate surface. For presentation purposes, panels (a) and (b) exhibit different background subtractions and the line scans in panel (b) are shifted in the vertical direction. Reprinted with permission from Ref. [26]. Copyright 2013 American Chemical Society.

ation density is influenced by the growth temperature and is independent of the amount of ceria, in accordance with basic nucleation theory [45]. Continued deposition of ceria only increases the size of the ceria islands and does not affect the nucleation density, again implying that it is mainly controlled by surface kinetics (see Section 3). Ceria grown at 900 °C at 4.5 ML of ceria shows the clear growth of large micrometer-sized particles (Fig. 2, also see movie in Supplementary material) [26]. These large islands appear with an almost perfect triangular shape, reflecting the three-fold symmetry of the fluorite lattice, and preferentially develop on substrate terraces, while the island density is strongly increased at step bunches, which are discernible as bright "bands" in the large-scale overview image (Fig. 2b). This decoration effect is due to an enhanced oxygen uptake in the stepped regions of the Ru(0001) crystal [46]. Hence, in this temperature regime the island nucleation density and their shape are determined both by the growth temperature and the surface morphology of the substrate (see Section 5).

The geometric structure of the ceria islands was determined by Flege et al. [25] using the low energy electron diffraction (LEED) pattern as shown in Fig. 3. The outer hexagonal ring consists of 6 sharp diffraction spots, which mark the first-order Bragg reflections of the Ru(0001) substrate. Furthermore, relatively weak half-order spots are discernible corresponding to the three-domain (2×1)-O adsorbate superstructure. In addition to these, the LEED pattern shows an inner hexagonal ring of ceria related $p(1.4 \times 1.4)$ superstructure spots, which result from the (111)-oriented fluorite crystal lattice [18,19]. These diffraction spots are found along the main-symmetry and lower symmetry directions of the substrate. Since these oxide patches preferentially lie along the same directions

as the substrate integer order maxima, there is a well-defined two-dimensional registry of the ceria islands with respect to the underlying substrate lattice. Furthermore, since the fluorite structure only exhibits a three-fold rotation axis, this configuration gives rise to the occurrence of rotational domains of ceria. Employing a diffracted beam with non-vanishing in-plane momentum transfer for so-called dark-field imaging, these rotational domains can clearly be mapped in real space (Fig. 3c), also allowing a determination of the amount of ceria minority particles whose in-plane lattice vectors are not aligned in parallel to the substrate.

After establishing the basic growth characteristics and the ceria island geometry with respect to the ruthenium support, we now turn to the morphology and crystallographic structure of the ceria particles.

3. Morphology and atomic structure

The ceria island morphology and atomic structure have been investigated by atomic force microscopy (AFM) (Fig. 4) [26] and STM (Fig. 5) [47]. Fig. 4a shows an AFM image of a ceria model catalyst prepared at 800 °C and at an oxygen partial pressure of 5×10^{-7} Torr (ceria coverage ~1 ML), comparable to the LEEM image displayed in Fig. 1f. The perfectly triangular islands are approximately 3 nm tall with very sharp edges (See line scans in Fig. 4b). The islands exhibit large, flat terraces and step edges that are significantly influenced by the step edges of the Ru substrate (also see Section 5). The ceria island triangles are not perfectly equilateral with two sides of the same lengths (isosceles) while the remaining side is shorter. This may indicate a non-negligible influence of the substrate even at this high growth temperature, where the morphology and shape can be expected to essentially represent the intrinsic structural properties of the ceria particles.

While the atomic structure of the ceria islands cannot be addressed by ex situ AFM under ambient conditions, they provide easy access to the "missing" third dimension in LEEM; also, they make an excellent bridge between the mesoscale LEEM and the nanoscale STM images that may additionally provide atomically resolved insights into the geometric and electronic surface structure of the ceria particles, including the nature of the defects.

A primary strength of the STM is the ability to probe the atomic structure of the surface of the ceria films, including individual point defects and other reactive sites, and has been demonstrated for $CeO_2(111)$ films prepared on a number of metallic substrates [48,49]. The results displayed in Fig. 5 were obtained by Jerratsch et al. in an ultrahigh vacuum STM operated at 10 K on a 1.5 nm (5 trilayer) thick ceria film on Ru(0001) [40]. This was prepared by depositing Ce onto a sputtered and annealed Ru(0001) surface in 5×10^{-6} mbar O_2, whereby half of the material was dosed at 100 K and half at 450 K. After annealing to 1000 K in O_2, the film displays a sharp $p(1.4 \times 1.4)$ LEED pattern that is characteristic for the $CeO_2(111)$ surface (cf. Fig. 3a) and bare areas of the substrate are visible between the ceria (Fig. 5a). Atomically resolved STM measurements are mainly obtained at positive sample bias (unoccupied states), where the Ce^{4+} cations are responsible for the contrast (Fig. 5b). At negative bias, the filled O 2p states govern the contrast (Fig. 5c); however, atomic resolution is more difficult to obtain. In both cases, the observed atom periodicity of 4.0 Å is consistent with the CeO_2 lattice constant of 3.83 Å. As the ceria films were prepared in an excess of O_2 they exhibit only a small defect concentration. Oxygen vacancies were therefore generated by exposure of the film to 50 eV electrons (1 mC dose) at 100 K. At positive sample bias (empty states), the surface oxygen vacancies appear as paired and tripled protrusions of ~0.4 Å height, which mark the Ce^{3+} ions around the vacancy (Fig. 5d and e). When an oxygen vacancy is formed, excess electrons remain in the surface resulting in two
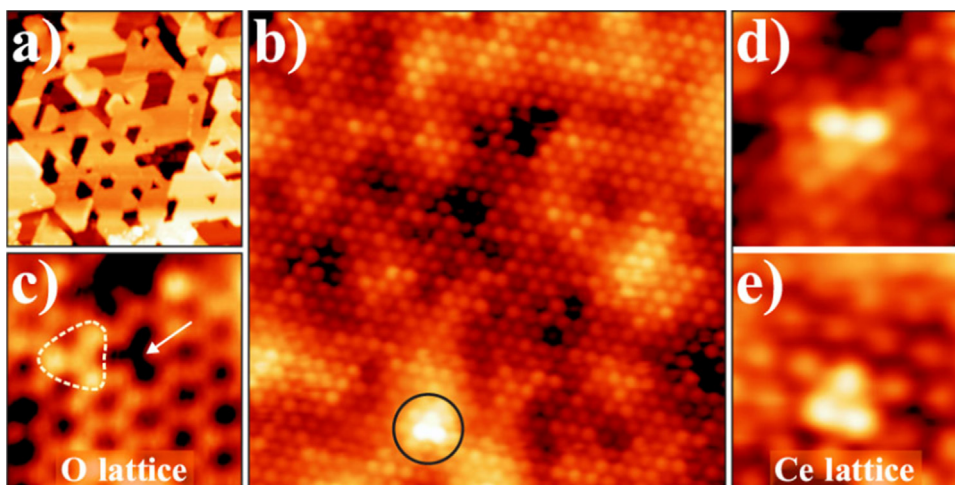
Fig. 5. (a) STM image of a 5 trilayer thick CeO_2 film grown on Ru(0001) (3.1 V, 100×100 nm^2) (b) Atomically resolved image showing the Ce sublattice (1.2 V, 12×12 nm^2). The protrusion in the lower part is assigned to a single O vacancy. (d), (e) Similar defects imaged with a tip configuration that is sensitive to the Ce lattice (1.2 V, 2.4×2.4 nm^2) and (c) to the O lattice (-2.2 V). The arrow in (c) marks a surface O vacancy, while the triangle denotes a subsurface defect characterized by three protruding O ions. Reprinted with permission from Ref. [47]. Copyright 2011 by the American Physical Society.

Ce^{4+} cations becoming reduced to Ce^{3+}. From the appearance in STM images (Fig. 5d and e), there is some variation in the localization of this excess charge although the precise position is still not clear, even with the evidence provided by scanning tunneling spectroscopy and DFT simulations. These Ce^{3+} sites do appear to play an important role in the nucleation of Au atoms on top of the ceria, and as such are of much interest for future studies of reactivity and support of metal nanoparticles [50]. At negative sample bias, the oxygen vacancies appear as dark atom-sized depressions, confirming their identity as a surface O vacancy (Fig. 5c, arrow) [11,51]. In addition to these, subsurface vacancies that appear as three protruding maxima at negative bias are occasionally observed (Fig. 5c, dashed triangle).

4. Thermodynamic and kinetic effects on growth

The effect of temperature on the growth process was carefully studied, with preparation of ceria islands at different temperatures. Fig. 6 shows this in a series of images with triangular shaped islands of ceria forming on the Ru(0001) substrate at temperatures between 970 K and 1270 K. This growth follows an Arrhenius-like dependence of island density on temperature. It is possible to obtain an activation energy of $E_A = 2.03 \pm 0.08$ eV from this trend [26].

The atomic structure of CeO_x islands grown at higher temperatures was also investigated using STM by Hasegawa et al. [52], where the terrace width and island size were observed to change drastically with growth temperatures of 1040 K and 1060 K (Fig. 7), in agreement with our previous findings from LEEM (Fig. 1). STM images of islands of differing thickness ($\sim$6 ML and $\sim$ 8 ML) with atomically flat and well-defined step edges are shown in Fig. 7(a and b). The inset of Fig. 7(a and b) shows a typical terrace with atomic resolution. Fig. 7(c) displays a moiré pattern observed on the second layer of the film indicating a lattice mismatch between the Ru substrate and the ceria layer. Fig. 7(d) is the corresponding LEED pattern for a ceria over layer prepared at 1060 K and an average island thickness of 2 ML. The ordered structure can be best described with the unit of the triangle superimposed in the STM image of Fig. 7(c). The unit has the periodicity of five times of the nearest neighbor (NN) distance of the oxygen atoms of the CeO_2(111) film. This result correlates well with the structure

of CeO_2(111)/Ru(0001) as determined from high-resolution LEED [26], which will be presented in the next section.

5. High-resolution LEED and interface analysis

In all of our LEED investigations of CeO_2(111)/Ru(0001), we observe p(1.4×1.4) spots, attributed to ceria. To get an even more detailed insight into reciprocal space structure and to reveal the structural origin of the p(1.4×1.4) phase, that is, whether it is commensurate or incommensurate, we obtained LEED with very low inelastic background [26] for a sample grown at 700 °C as displayed in Fig. 8a. A magnified view of the region enclosed by white lines in Fig. 8a is displayed in Fig. 8b. As expected, the LEED pattern exhibits the six-fold symmetric Ru(0001)-(1×1) diffraction spots (black circles) as well as the well-known p(1.4×1.4) ceria spots (red circles). A p(2×1)-O phase with an additional splitting due to antiphase domain boundaries is also visible (blue ellipse). Diffraction spots belonging to rotated ceria domains occur at positions highlighted by red circular lines. The most important observation from Fig. 8 however is the presence of the small (n/7) spots, whose positions are marked by small black dots. These diffraction peaks are observed for the first time, probably due to the superior resolution and sensitivity of the energy-filtered LEEM instrument as compared to a conventional LEED system. Since the (n/7) spots all exhibit comparable intensities, we do not observe the characteristic, damped envelope function typical of a moiré pattern, which would indicate a coincidence lattice for ceria on Ru(0001). This observation clearly reveals that ceria on Ru(0001) develops a (7×7) superstructure and is therefore commensurate. The (5/7) spots exhibit the highest intensity because they coincide with the (1×1) diffraction spots of bulk CeO_{2-d}(111). The LEED pattern can, therefore, be explained by a superposition of the diffraction from $CeO_{2-\delta}$(111)-type islands and from regions where the islands are sufficiently thin that we can still probe the (7×7) superstructure at the interface between the ceria and substrate. The presence of commensurateness implies that the atomic interface between the ceria islands and the ruthenium substrate is well-ordered and coherent.

6. Carpet growth mechanism

The presented LEEM studies support a mechanism of growth that is a carpet-like model for the ceria islands as proposed by Flege et al. [25]. This is depicted schematically in Fig. 9. This carpet-like
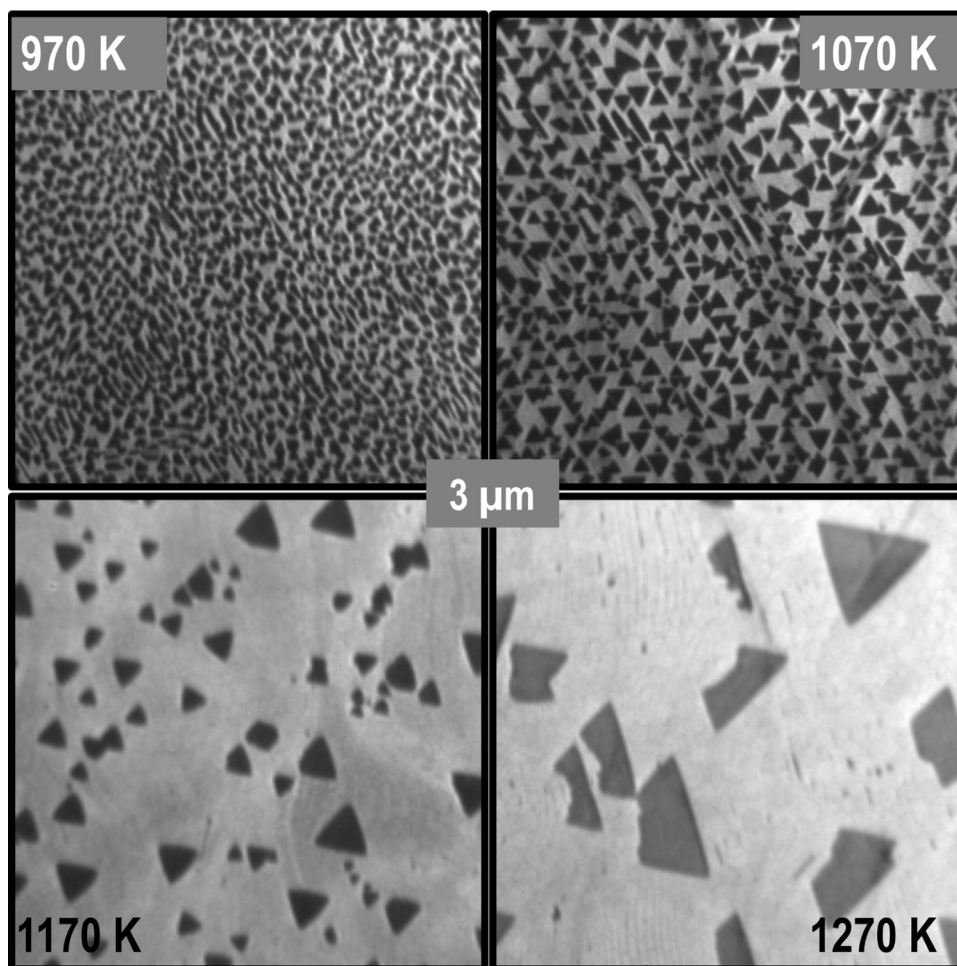
Fig. 6. LEEM images ($3 \times 3\,\mu m^2$) of growth at 970, 1070, 1170 and 1270 K of CeO$_x$ on to a Ru (0001) substrate. The ceria islands appear as dark shapes on the bright Ru substrate.

growth is a result of the balance between the strain energy of the elastically distorted oxide film in more densely-stepped areas of the substrate and the oxide-substrate interaction energy in the flat regions. When the "easy" growth direction coincides with the local substrate step orientation as defined by its outward normal, the continuation of the oxide structure over the step results in a larger separation of the oxide film from the lower substrate terrace in the vicinity of the step (Fig. 9d). This scenario implies that the stiffness of the oxide film prevents it directly following the curvature of the substrate topography, which reduces the interaction with the underlying substrate. The additional elastic deformation energy and the reduced interaction energy with the substrate together contribute to a net increase in the total energy per unit oxide film area. Even in the absence of any additional kinetic effects, this increase in total energy results in a substantial effective activation energy for growth over a step edge. Consequently, when the step height is too large, as encountered for step bunches on the Ru surface, the elastically deformed area and associated strain energy is large, inhibiting overgrowth as shown in Fig. 9(e). Similarly, when a straight ceria island edge encounters a step with parallel-oriented outward normals (see Fig. 9(c)), then the area that needs to be deformed is also large, again hindering further growth in this direction. This carpet-like growth mode has previously been proposed for thin NaCl films on Ge(100) [53] based on spot-profile analysis LEED investigations [54]. This observation suggests that this growth mode may be considered a rather general feature of strongly ionic binary films, which have only a moderate interaction with the substrate. Supporting this is the observation that seemingly unrestricted carpet-like growth is found for graphene on single [55] [48] and polycrystalline [56,57] ruthenium surfaces. The well-established strong interaction between graphene and ruthenium emphasizes that the energy balance between strain energy and film-substrate interaction energy is critical to the behavior during growth. Further support for the carpet-growth model is provided by the behavior around substrate step bunches and grain boundaries, which are significant obstacles for lateral overgrowth by the oxide. Interestingly, this results in the evolution of irregular island shapes, even approaching quasi-linear, stripe-like structures for oxide islands that have nucleated near substrate step bunches.

In the previous sections we have established a comprehensive picture of the ceria growth characteristics on the Ru(0001) surface by reactive MBE techniques. This intimate knowledge not only allows tailoring the nanoscale morphology and atomic structure to the targeted application, but also a clear strategy to identifying key structural features and link them with the chemical reactivity, thereby providing a well-defined route to unraveling the structure-function relation in ceria-based catalytic chemistry.

7. Chemical state and reactivity

The most common method for determining the oxidation state of the cerium cation within ceria is *via* X-ray photoemission spectroscopy of the Ce 3d, 4d, or 4f levels. An example from Flege et al. [25] of such an identification of the chemical state of the ceria
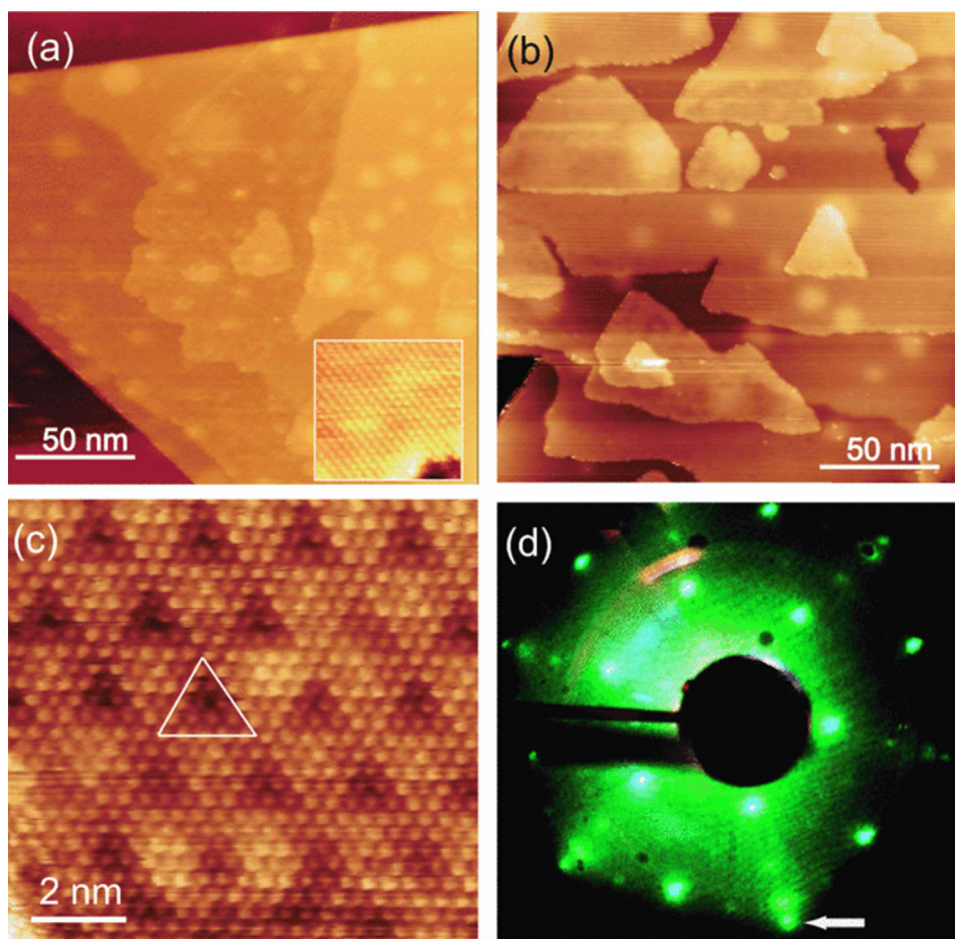
Fig. 7. (a-b) Ceria film grown at 1040 K (a) and 1060 K (b) in an oxygen background of 5×10^{-7} Torr. The thicknesses of the majority of the islands are (a) 6 ML and (b) 8 ML. (c) Magnified image of the terrace, which is 2 ML high from the metal surface. A moiré pattern with 5×5 periodicity with respect to the $CeO_2(111)$ surface is marked by a white triangle. (d) LEED pattern observed for the surface of (c). A spot corresponding to the moiré superstructure is marked by an arrow. Reprinted with permission from Ref. [52]. Copyright 2014, AIP Publishing LLC.
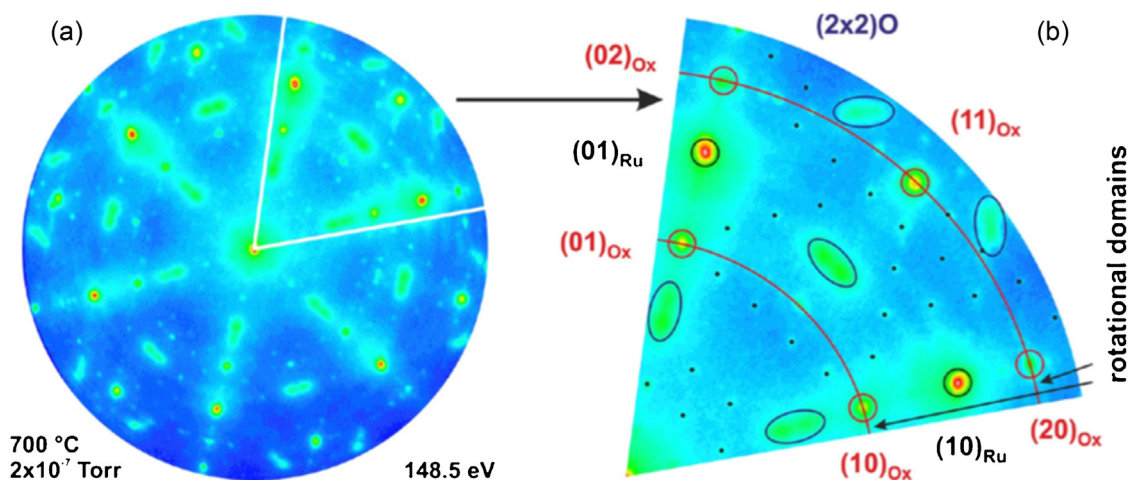

Fig. 8. LEED image of highly oxidized ceria grown at a 700 °C substrate temperature and an oxygen partial pressure of 2×10^{-7} Torr. Panel (b) shows a magnified part of the LEED pattern. The LEED pattern exhibits intense Ru(0001) substrate spots and the p(1.4 × 1.4) ceria phase with an additional (7 × 7) superstructure which is highlighted by small black dots. A p(2 × 1)O phase is observed with an additional splitting of the diffraction spots due to the presence of antiphase domain boundaries. The thin red circular lines highlight possible positions for ceria rotational domains that may be found at this growth temperature. Reprinted with permission from Ref. [26]. Copyright 2013 American Chemical Society. (For interpretation of the references to colour in this figure legend, the reader is referred to the web version of this article.).

islands using energy-filtered XPEEM at the Ce 4d core level is shown in Fig. 10a, comparing a fully oxidized CeO_2 film (red line) and a partially reduced CeO_x film (blue line). It is possible to derive the oxidation state of ceria by comparing the peak intensities of the peaks W‴ and X‴ with the intensity of the remaining spectrum [58]. Fig. 10a shows the background-corrected Ce 4d spectrum of
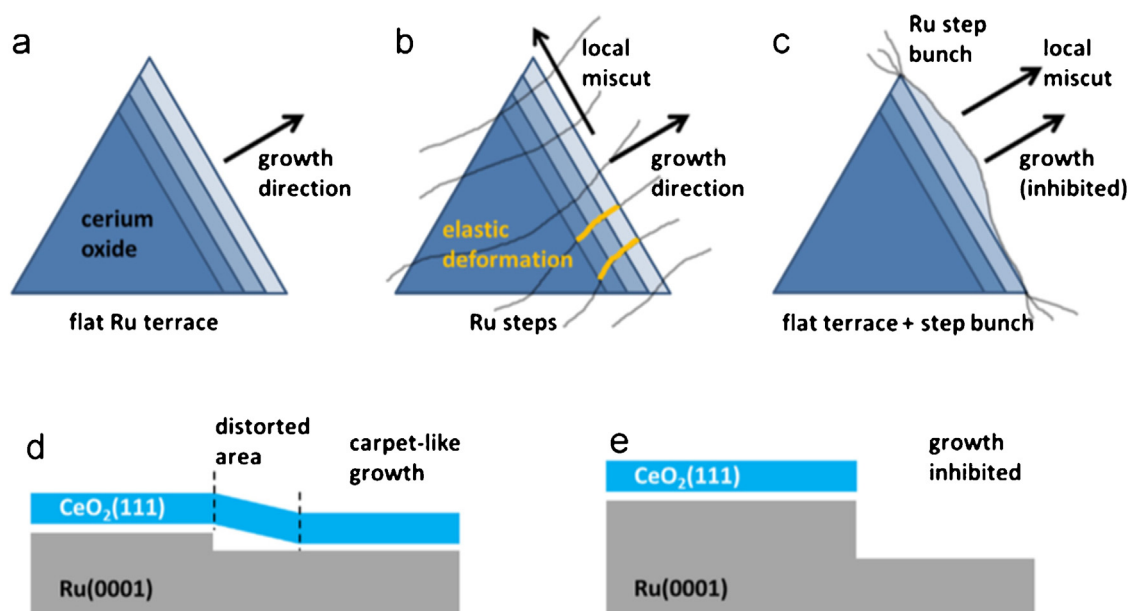
Fig. 9. Schematic of the carpet growth model for CeO$_2$(111) on Ru(0001). (a) Unperturbed growth of ceria adopting the shape of equilateral triangles on (a) an infinitely flat terrace and (b) on a stepped surface with the local miscut oriented perpendicular to the main island growth direction. (c) Inhibited ceria island growth due to parallel alignment of growth direction and local substrate miscut orientation. (d) Carpet-like growth over low substrate steps. (e) Inhibited growth over high substrate steps. Reprinted from Ref. [25], with permission from Elsevier.
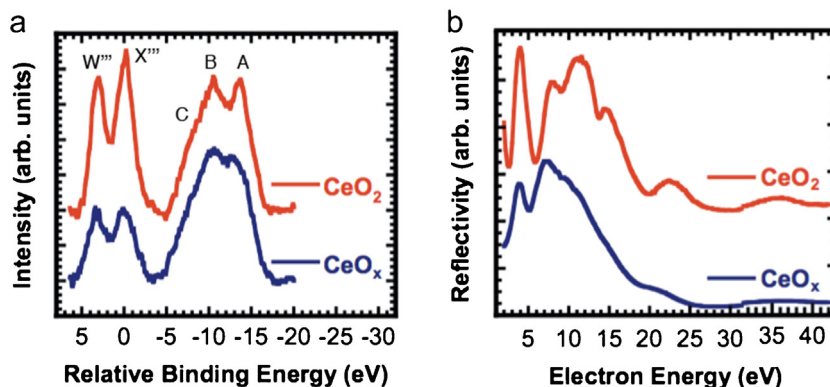

Fig. 10. (a) Ce 4d soft x-ray photoemission (hv = 165 eV) and (b) corresponding $I(V)$-LEEM spectra collected for nearly fully oxidized ceria (CeO$_2$) and moderately reduced ceria (CeO$_x$) prepared on Ru(0001). Reprinted from Ref. [25], with permission from Elsevier. (For interpretation of the references to colour in this figure legend, the reader is referred to the web version of this article.).

a sample grown at 1100 K in 5 × 10^{-7} Torr O$_2$ (red line). Due to the typical lower resolution of the photoelectron spectra acquired in XPEEM mode as compared to available high-resolution X-ray photoelectron spectra [59], the peaks are slightly broader than usual. From the relative intensity distribution of the peaks W''' and X''' compared to peaks A–C, we can conclude that the ceria is nearly fully oxidized under these growth conditions. The blue line in Fig. 10a shows the Ce 4d spectrum after background subtraction, of a sample grown at 630 K in 1 × 10^{-8} Torr O$_2$. Here, we find that the peaks W''' and X''' contribute far less intensity to the spectrum, illustrating a lower oxidation state of ceria that is consistent with the less oxidative conditions during the film growth. Fig. 10b shows the $I(V)$-LEEM spectra for the two films probed with X rays in Fig. 10a, and illustrates how the fine structure in the $I(V)$ curve also allows us to identify the oxidation state of the ceria. The red and blue lines, corresponding to the fully and partially oxidized films, respectively, clearly display significant differences.

In general, the analysis of $I(V)$-LEEM data follows two different procedures. In the first, the $I(V)$ curves are used to provide a fingerprint to identify the local atomic structure by comparing with experimentally obtained $I(V)$ curves from reference structures. Yet, a more complex interpretation may be achieved by comparing the experimental $I(V)$ curves to theoretical reflectivity spectra that have been calculated within an *ab initio* scattering theory that takes into account the unoccupied complex band-structure of the model catalyst [60]. However, for correlated electron systems such as ceria this analysis is very complex, currently prohibiting the analysis of trial structures with a large number of basis atoms per unit cell [43]. Yet, even qualitatively it is clear that the $I(V)$ curve changes upon change in average oxidation state, which directly implies that $I(V)$ spectra can be used as local probes within an oxidation state analysis with the nanometer spatial resolution provided by the LEEM technique.

An alternative method for determination of the ceria oxidation state with X-ray photoemission techniques is *via* X-ray absorption spectroscopy, often of the Ce M$_{4,5}$ edge whose appearance is particularly sensitive to changes in the electronic configuration of the cation. One advantage of this method, especially when employed in combination with XPEEM, is the improved signal-to-noise ratio, which directly results in improved lateral resolution and shorter
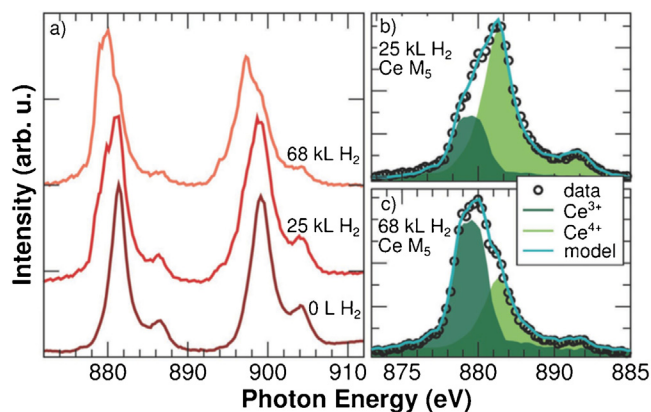
Fig. 11. (a) Ce M4,5 X-ray absorption spectra acquired from an individual ceria microparticle in XPEEM during the reaction with H_2. Bottom: the initial CeO_2. Center: after dosing 25 kL H_2 at 700 K. Top: after 68 kL H_2 at 700 K. (b,c) Fitting of the Ce M5 edge by a linear combination of Ce^{3+} (dark green) and Ce^{4+} (light green) related peaks. Reprinted from Ref. [61], with permission. (For interpretation of the references to colour in this figure legend, the reader is referred to the web version of this article.).

image acquisition times, although this comes at the sacrifice of some of the surface sensitivity as compared to the XPS method displayed in Fig. 10. Fig. 11 shows the evolution of the XAS spectra obtained by Höcker et al. [61] from a single ceria nanoparticle with increasing exposure to H_2. μ-XAS of the as-prepared island (bottom spectrum in Fig. 11a) indicates that the microparticle is nearly fully oxidized (CeO_2), which is homogeneous across the island [61]. After dosing 25 kL of hydrogen at a sample temperature of 430 °C, however, additional peaks are observed on the lower energy side of both the M4 and M5 edges, consistent with Ce^{3+} formation [62,63]. The spectrum is still dominated by the Ce^{4+} peaks, showing that the complete particle is only mildly reduced, indicating that the reduction by H_2 is a slow, activated process. This observation suggests the presence of a considerable kinetic barrier for H_2 dissociation over $CeO_2(111)$, a finding which disagrees with earlier calculations that predicted a barrier of only 0.2 eV [64]. However, better agreement is found with recent DFT studies that predict a kinetic barrier of about 1 eV, attributed to a slow dissociation step of the chemisorbed H_2 molecule into separate hydroxyl groups [65,66]. To derive the oxidation state of the ceria from the Ce M5-edge XAS data, we applied a linear combination of the Ce^{4+} and Ce^{3+} peaks [62] as shown in Fig. 11b,c. This yielded a stoichiometry of $CeO_{1.85}$ after dosing 25 kL hydrogen (Fig. 11b) and $CeO_{1.68}$ after dosing of an additional 43 kL of H_2 (Fig. 11c).

In order to probe any changes in the surface structure of the ceria that accompany the reduction process in H_2, μ-LEED was conducted [61] on single particles with an incident electron beam size of 500 nm. This procedure is depicted in Fig. 12; the changes in the LEED pattern from an individual particle (as marked in the inset of Fig. 12a) recorded in real-time are presented as a time-lapse sequence in Fig. 12a–d. Before hydrogen is introduced, only the (1×1) integer spots of $CeO_2(111)$ (Fig. 12a) are observable. After dosing 500 L of H_2 at 5×10^{-7} mbar, additional spots emerge (Fig. 12b), which are a direct consequence of the local ordering of the oxygen vacancies resulting from dissociative adsorption of H_2 and subsequent surface reduction. These superstructure spots remain constantly visible throughout the reduction process, indicating that the surface remains crystallographically ordered at all times. The superstructure spots (Fig. 12b) have a periodicity of 2.6 with respect to the integer spots of CeO_2. This period is dependent on both the H_2 pressure and dose. Increasing the pressure to 1×10^{-6} mbar induces larger periodicities, resulting in a commensurate (3×3) superstructure (Fig. 12c), which remains unchanged upon subsequent dosing at this pressure. However, at a H_2 pressure of 2×10^{-6} mbar the superstructure spots move apart and finally appear at the (1/4) and (3/4) positions as shown in

Fig. 12d. This coincides with the emergence of a stationary spot at the (1/2) position, which together with the satellite spots results in a (4×4) periodicity. Quantitatively, this is concomitant with a slight in-plane lattice expansion of about $(1 \pm 0.3)\%$ with respect to the as-prepared $CeO_2(111)$. The (4×4) pattern is attributed to the formation of the bixbyite $Ce_2O_3(111)$ phase, composed entirely of Ce^{3+} [67], whereas the (3×3) periodicity has previously been attributed to a stable ceria phase with stoichiometry $CeO_{1.67}$ [68]. Interestingly, a much higher H_2 dose is required for significant reduction as measured by μ-XAS than to reach full reduction in the μ-LEED experiments. This observation is explained by considering the completely different probing depths of the two methods. While LEED at 40 eV kinetic energy probes just a few tenths of a nanometer into the sample, the escape depth of the very slow electrons (2.6 eV) in XAS is orders of magnitude larger, thus revealing an oxygen concentration gradient within the ceria islands.

In order to explore the effects of chemical reduction of $CeO_2(111)/Ru(0001)$, we have exposed a film to methanol at 300 K, followed by gentle annealing [60]. A LEEM image of the as-prepared $CeO_2(111)$ islands on $Ru(0001)$ is displayed in Fig. 13a. In the image, all of the ceria islands appear homogeneously bright, suggesting a uniform oxidation state after growth. After methanol exposure and annealing, however, significant intensity variations are observed across the surface of the ceria islands (Fig. 13b). This image contrast, whose chemical interpretation is corroborated by the presence of distinct local $I(V)$ curves [60], clearly indicates a local variation in oxidation state although interestingly the brighter and darker patches show no apparent relation to the island shape or size.

To provide a comparison to the reduction by methanol displayed in Fig. 13, which shows clear heterogeneity across the ceria islands as the reaction progresses, the reduction of the ceria by H_2, previously examined spectroscopically in Figs. 11 and 12, was probed with high resolution LEEM imaging, the results of which are displayed in Fig. 14 [61]. After partial reduction by H_2, the ceria microparticles (dark at these imaging conditions) do not exhibit a homogeneous intensity (also see inset of Fig. 12a, which has been taken at virtually identical imaging conditions as Fig. 13) but display two distinct levels of intensity (Fig. 14a). With further hydrogen exposure, this bimodal contrast completely disappears. The local $I(V)$ reflectivity curves, which are directly linked to the local surface structure [43] and stoichiometry [60], are used to identify and separate the two domains on the nanometer scale. (Fig. 14b) Comparison to reference spectra for Ce_2O_3 (bixbyite), $CeO_x(3 \times 3)$, and CeO_2 (fluorite) reveals that the areas appearing dark in Fig. 14a at 16.2 eV can be assigned to $Ce_2O_3(111)$ whereas the brighter particle areas indicate the $CeO_x(3 \times 3)$ phase (Fig. 14b). After exposure
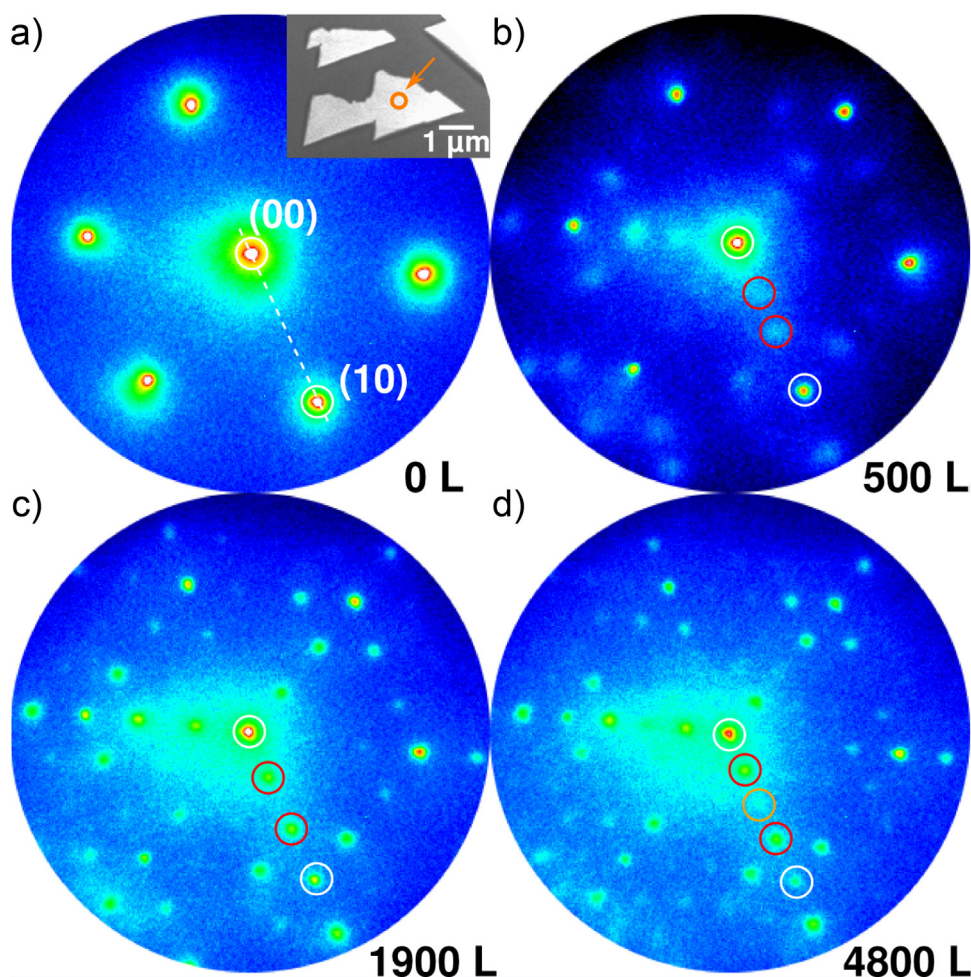
Fig. 12. (a–d) μ-LEED images obtained during the chemical reduction of a single ceria particle by hydrogen (exposures quoted in Langmuirs) at 700 K. White circles indicate the reflections of CeO$_2$. The positions of the superstructure spots are indicated by red (moving spots) and orange circles (stationary half-order spot). (a) Inset: LEEM image of the surface (E = 15.3 eV). The orange circle indicates the electron beam spot size and position during the reduction experiment. Reprinted from [61], with permission. (For interpretation of the references to colour in this figure legend, the reader is referred to the web version of this article.).
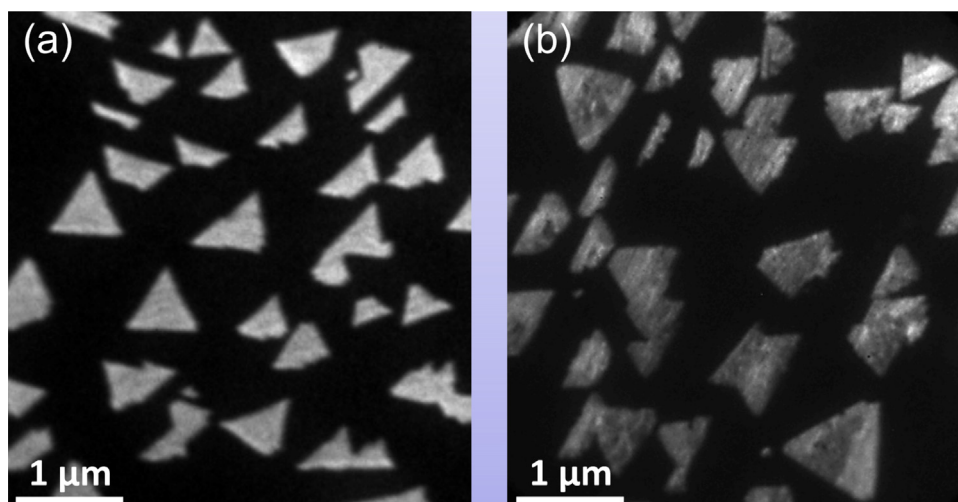

Fig. 13. LEEM images (E = 15.4 eV) recorded (a) after growth and (b) after reduction by exposure to methanol subsequent annealing. The contrast on the ceria islands is due to local varying stoichiometry. Adapted with permission from Ref. [60]. Copyrighted by the American Physical Society.

for several hours to 2×10^{-6} mbar H$_2$, the variable contrast within the ceria particles vanishes and the *I*(*V*) curve shows the expected fully reduced Ce$_2$O$_3$(111) fingerprint.

8. Future prospects of probing *In situ* reactivity

The ability to dynamically observe reactions as they occur over the surfaces of catalysts is essential to the clear and
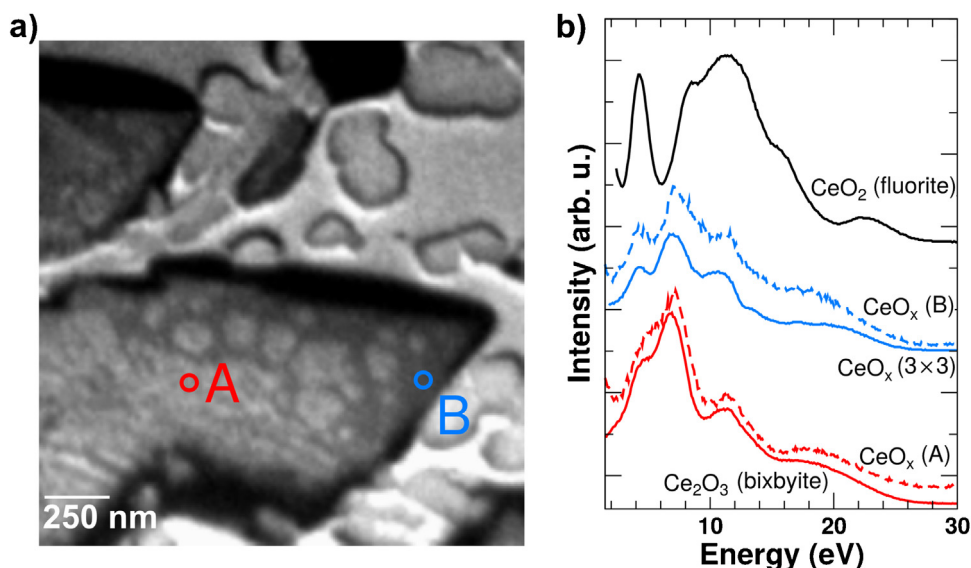
Fig. 14. (a) LEEM image (E = 6.2 eV) of a ceria film after reduction by hydrogen showing inhomoguous reduction of the cerium oxide particles. (b) $I(V)$ fingerprints recorded from highlighted areas "A" and "B" (dashed lines) and compared to $I(V)$ reference spectra (solid lines). The bright patches in panel (a) appear upon prolonged H_2 exposure and, based on $I(V)$ and μ-LEED analysis, are consistent with local hydrogen incorporation. Reprinted from Ref. [61], with permission.

unambiguous establishment of active ingredients and insights into the mechanism of reactions. Static microscopy or spatially averaged spectroscopy or scattering is certainly important yet is limited to inference or extrapolation of the active state of the catalyst, often before or after reaction has taken place. The degree of surface heterogeneity that results and often accompanies such processes is a major obstacle to many methods. Direct causality where a reactant is activated and converted to a product over a specific surface site or region is thus challenging and is ultimately the '*holy grail*' in being able to implicate the true nature of catalysts and reactions.

Efforts to study *in situ* surface reactivity are therefore clearly motivated by a need to take images, spectroscopy and scattering in a rapid, time-dependent, and spatially resolved manner under the appropriate reaction conditions. Combing all three of these parameters into one *in situ* method applied in real time may only be possible with a combination of LEED/LEEM/X-PEEM, where correlative local area diffraction, fast images and X-ray spectroscopy can be brought to bear towards the probe of a simple reaction. This has been demonstrated for the first time in the case of CeO_x-Ru (Fig. 15) under reaction with H_2 in real-time. The H—H activation is especially important for reactions including CO_2 and olefin hydrogenation for conversion to alcohols and oligomers, respectively. It was possible to identify reduced phases as they evolve on the surface of the CeO_x and which were identified with local area electron diffraction and X-ray spectroscopy. Together with time-resolved I(V)-LEEM, this experimental methodology is also able to unravel *cooperative effects* as, *e.g.*, in reactant spillover over oxygen-rich Ru(0001) surfaces [69,70], whose oxidation we have also followed from submonolayer oxygen coverages to formation of the bulk-like oxide phases [71,72]. Hence, the full tool set for spatially resolved monitoring of different cerium oxidation states as well as of the ruthenium support at various levels of oxidation during redox reactions over ceria/Ru surfaces is readily available, offering the exciting possibility to address complex reactions involving dynamic transformations of all surface components in the catalytic reaction.

The ability to perform this methodology beyond just single reactants and in fact with near operando catalytic reactions is not yet realized, but is the future prospect for advanced characterization of surface reactions in real time. The CeO_x-Ru(0001) system, now with a large body of work aimed at its fundamental characterization of its growth and local chemical state, will
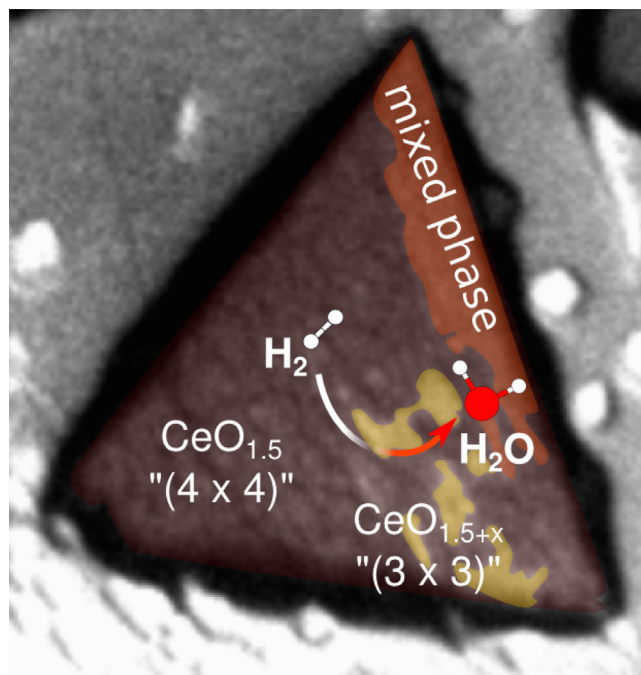

Fig. 15. In situ LEEM/PEEM image of CeO_x-Ru(0001) island under H_2 activation, showing regions of surface structure evolve as a function of H_2 activation in real time.

be an important benchmark for such studies. A near atomic level model of structural changes that occur during a reaction may be obtainable while under steady state and pulsed reactant conditions. In addition, spectroscopy coupled to atomic structure may also be very helpful in identifying reaction mechanisms where C, O containing adsorbates that accumulate on surface sites could be identified. Intentional perturbation of the surface atomic geometry either as grown or with pre-treatments can also be tested systematically to further establish design principles under which reactant-substrate transformations may occur leading to optimum or destructive transformations (deactivation).

9. Conclusions

The CeO_x-Ru(0001) surface can be prepared by reactive molecular beam epitaxy to yield well-defined (111)-oriented nano-islands, micron-sized particles, and continuous films that allow for the investigation of the unique properties of cerium oxide. The atomic structure and chemical state have been well characterized with STM and LEEM/LEED with a clear perspective of the atomic arrangement of the last layer of O—Ce—O atoms and the defect states that prevail. Chemical states of the surface (Ce^{4+} *vs* Ce^{3+}) has been identified using X-ray methods such as XPS, XAS and X-PEEM and compared to *I*(*V*)-LEEM reflectivity data. The growth mode of ceria overlayers on Ru(0001) was established through dynamic LEEM studies and identified as a carpet-mode of growth, transforming into different surface architectures dependent on the oxygen potential and thermodynamics. The reactivity of the CeO_x-Ru(0001) surface was studied upon reaction with methanol and H_2, with interesting structural transformations that predominantly favored reduced surface state during the activation of reactants. The CeO_x-Ru(0001) system stands out as an important prototype model system for the understanding of ceria catalytic chemistry.

Acknowledgements

Appendix A. Supplementary data

Supplementary data associated with this article can be found, in the online version, at http://dx.doi.org/10.1016/j.apcatb.2016.02.043.

References

[1] Q. Fu, H. Saltsburg, M. Flytzani-Stephanopoulos, Active nonmetallic Au and Pt species on ceria-based water-gas shift catalysts, Science 301 (2003) 935–938.

[2] J.A. Rodriguez, S. Ma, P. Liu, J. Hrbek, J. Evans, M. Pérez, Activity of CeO_x and TiO_x nanoparticles grown on Au(111) in the water-gas shift reaction, Science 318 (2007) 1757–1760.

[3] K. Ding, A. Gulec, A.M. Johnson, N.M. Schweitzer, G.D. Stucky, L.D. Marks, P.C. Stair, Identification of active sites in CO oxidation and water-Gas shift over supported Pt catalysts, Science 350 (2015) 189–192.

[4] A. Martínez-Arias, D. Gamarra, M. Fernández-García, A. Hornés, P. Bera, Z. Koppány, Z. Schay, redox-catalytic correlations in oxidised copper-ceria CO-PROX catalysts, Catal. Today 143 (2009) 211–217.

[5] Y. Ji, J.-S. Choi, T.J. Toops, M. Crocker, M. Naseri, Influence of ceria on the NO_x storage/reduction behavior of lean NO_x trap catalysts, Catal. Today 136 (2008) 146–155.

[6] J. Graciani, K. Mudiyanselage, F. Xu, A.E. Baber, J. Evans, S.D. Senanayake, D.J. Stacchiola, P. Liu, J. Hrbek, J.F. Sanz, J.A. Rodriguez, Highly active copper-ceria and copper-ceria-titania catalysts for methanol synthesis from CO_2, Science 345 (2014) 546–550.

[7] G. Vilé, S. Colussi, F. Krumeich, A. Trovarelli, J. Pérez-Ramírez, Opposite face sensitivity of CeO_2 in hydrogenation and oxidation catalysis, Angew. Chem. Int. Ed. 53 (2014) 12069–12072.

[8] Y. Lykhach, T. Staudt, M.P.A. Lorenz, R. Streber, A. Bayer, H.-P. Steinrück, J. Libuda, Microscopic insights into methane activation and related processes on Pt/Ceria model catalysts, ChemPhysChem 11 (2010) 1496–1504.

[9] G. Zhou, L. Barrio, S. Agnoli, S.D. Senanayake, J. Evans, A. Kubacka, M. Estrella, J.C. Hanson, A. Martínez-Arias, M. Fernández-García, J.A. Rodriguez, High activity of $Ce_{1-x}Ni_xO_{2-y}$ for H_2 production through ethanol steam reforming: tuning catalytic performance through metal-oxide interactions, Angew. Chem. Int. Ed. 49 (2010) 9680–9684.

[10] J.-D. Cafun, K.O. Kvashnina, E. Casals, V.F. Puntes, P. Glatzel, Absence of Ce^{3+} sites in chemically active colloidal ceria nanoparticles, ACS Nano 7 (2013) 10726–10732.

[11] F. Esch, S. Fabris, L. Zhou, T. Montini, C. Africh, P. Fornasiero, G. Comelli, R. Rosei, Electron localization determines defect formation on ceria substrates, Science 309 (2005) 752–755.

[12] A. Bruix, J.A. Rodriguez, P.J. Ramírez, S.D. Senanayake, J. Evans, J.B. Park, D. Stacchiola, P. Liu, J. Hrbek, F. Illas, A new type of strong metal-Support interaction and the production of H_2 through the transformation of water on Pt/CeO_2(111) and Pt/CeO_x/TiO_2(110) catalysts, J. Am. Chem. Soc. 134 (2012) 8968–8974.

[13] L.J. Burcham, M. Badlani, I.E. Wachs, The origin of the ligand effect in metal oxide catalysts: novel fixed-bed in situ infrared and kinetic studies during methanol oxidation, J. Catal. 203 (2001) 104–121.

[14] X.-P. Wu, X.-Q. Gong, Unique electronic and structural effects in vanadia/ceria-catalyzed reactions, J. Am. Chem. Soc. 137 (2015) 13228–13231.

[15] S.Y. Yao, W.Q. Xu, A.C. Johnston-Peck, F.Z. Zhao, Z.Y. Liu, S. Luo, S.D. Senanayake, A. Martinez-Arias, W.J. Liu, J.A. Rodriguez, Morphological effects of the nanostructured ceria support on the activity and stability of CuO/CeO_2 catalysts for the water-gas shift reaction, Phys. Chem. Chem. Phys. 16 (2014) 17183–17195.

[16] S. Luo, T.-D. Nguyen-Phan, A.C. Johnston-Peck, L. Barrio, S. Sallis, D.A. Arena, S. Kundu, W. Xu, L.F.J. Piper, E.A. Stach, D.E. Polyansky, E. Fujita, J.A. Rodriguez, S.D. Senanayake, Hierarchical heterogeneity at the CeO_x–TiO_2 interface: electronic and geometric structural influence on the photocatalytic activity of oxide on oxide nanostructures, J. Phys. Chem. C 119 (2015) 2669–2679.

[17] D.J. Stacchiola, S.D. Senanayake, P. Liu, J.A. Rodriguez, Fundamental studies of well-defined surfaces of mixed-metal oxides: special properties of MO_x/TiO_2(110) {M = V Ru, Ce, or W}, Chem. Rev. 113 (2013) 4373–4390.

[18] D.R. Mullins, P.V. Radulovic, S.H. Overbury, Ordered cerium oxide thin films grown on Ru(0001) and Ni(111), Surf. Sci. 429 (1999) 186–198.

[19] J.L. Lu, H.J. Gao, S. Shaikhutdinov, H.J. Freund, Morphology and defect structure of the CeO_2(111) films grown on Ru(0001) as studied by scanning tunneling microscopy, Surf. Sci. 600 (2006) 5004–5010.

[20] N. Nilius, S.M. Kozlov, J.-F. Jerratsch, M. Baron, X. Shao, F. Viñes, S. Shaikhutdinov, K.M. Neyman, H.-J. Freund, Formation of one-dimensional electronic states along the step edges of CeO_2(111), ACS Nano 6 (2012) 1126–1133.

[21] L. Kundakovic, D.R. Mullins, S.H. Overbury, Adsorption and reaction of H_2O and CO on oxidized and reduced Rh/CeO_x(111) surfaces, Surf. Sci. 457 (2000) 51–62.

[22] S.H. Overbury, D.R. Mullins, D.R. Huntley, L. Kundakovic, Chemisorption and reaction of sulfur dioxide with oxidized and reduced ceria surfaces, J. Phys. Chem. B 103 (1999) 11308–11317.

[23] D.R. Mullins, S.D. Senanayake, T.L. Chen, Adsorption and Reaction of C_1C_3 alcohols over CeO_x(111) Thin Films, J. Phys. Chem. C 114 (2010) 17112–17119.

[24] S.M.F. Shahed, T. Hasegawa, Y. Sainoo, Y. Watanabe, N. Isomura, A. Beniya, H. Hirata, T. Komeda, STM and XPS study of CeO_2(111) reduction by atomic hydrogen, Surf. Sci. 628 (2014) 30–35.

[25] J.I. Flege, B. Kaemena, S.D. Senanayake, J. Höcker, J.T. Sadowski, J. Falta, Growth mode and oxidation state analysis of individual cerium oxide islands on Ru(0001), Ultramicroscopy 130 (2013) 87–93.

[26] B. Kaemena, S.D. Senanayake, A. Meyer, J.T. Sadowski, J. Falta, J.I. Flege, Growth and morphology of ceria on ruthenium (0001), J. Phys. Chem. C 117 (2013) 221–232.

[27] Y. Pan, N. Nilius, C. Stiehler, H.-J. Freund, J. Goniakowski, C. Noguera, Ceria nanocrystals exposing wide (100) facets: structure and polarity compensation, Adv. Mater. Interfaces 1 (2014).

[28] T. Duchoň, F. Dvořák, M. Aulická, V. Stetsovych, M. Vorokhta, D. Mazur, K. Veltruská, T. Skála, J. Mysliveček, I. Matolínová, V. Matolín, Comment on ordered phases of reduced ceria as epitaxial films on Cu(111), J. Phys. Chem. C 118 (2014) 5058–5059.

[29] D.A. Chen, J.S. Ratliff, X. Hu, W.O. Gordon, S.D. Senanayake, D.R. Mullins, Dimethyl methylphosphonate decomposition on fully oxidized and partially reduced ceria thin films, Surf. Sci. 604 (2010) 574–587.

[30] F.C. Calaza, T.L. Chen, D.R. Mullins, S.H. Overbury, Structure and reactivity of alkyl ethers adsorbed on CeO_2(111) model catalysts, Top. Catal. 54 (2011) 56–69.

[31] J. Zhou, A.P. Baddorf, D.R. Mullins, S.H. Overbury, Growth and characterization of Rh and Pd nanoparticles on oxidized and reduced CeO_x(111) thin films by scanning tunneling microscopy, J. Phys. Chem. C 112 (2008) 9336–9345.

[32] Y. Zhou, J. Zhou, Interactions of Ni nanoparticles with reducible CeO_2(111) thin films, J. Phys. Chem. C 116 (2012) 9544–9549.

[33] S.D. Senanayake, J. Zhou, A.P. Baddorf, D.R. Mullins, The reaction of carbon monoxide with palladium supported on cerium oxide thin films, Surf. Sci. 601 (2007) 3215–3223.

[34] Y. Pan, Y. Cui, C. Stiehler, N. Nilius, H.-J. Freund, Gold adsorption on CeO_2 thin films grown on Ru(0001), J. Phys. Chem. C 117 (2013) 21879–21885.

[35] J.I. Flege, W.X. Tang, M.S. Altman, Low-energy electron microscopy, in: E.N. Kaufmann (Ed.), Characterization of Materials, John Wiley & Sons, Inc., Hoboken, U.S, 2012.

[36] E. Bauer, Low energy electron microscopy, Rep. Prog. Phys. 57 (1994) 895.

[37] E. Bauer, Surface Microscopy with Low Energy Electrons, Springer, New York, U.S, 2014.

[38] M.S. Altman, W.F. Chung, C.H. Liu, LEEM phase contrast, Surf. Rev. Lett. 5 (1998) 1129.

[39] A.B. Pang, T. Müller, M.S. Altman, E. Bauer, Fourier optics of image formation in LEEM, J. Phys. Condens. Matter 21 (2009) 314006.

[40] S.M. Schramm, A.B. Pang, M.S. Altman, R.M. Tromp, A contrast transfer function approach for image calculations in standard and aberration-corrected LEEM and PEEM, Ultramicroscopy 115 (2012) 88–108.

[41] J.I. Flege, A. Meyer, J. Falta, E.E. Krasovskii, Self-limited oxide formation in Ni(111) oxidation, Phys. Rev. B 84 (2011) 115441.

[42] A. Locatelli, E. Bauer, Recent advances in chemical and magnetic imaging of surfaces and interfaces by XPEEM, J. Phys. Condens. Matter 20 (2008) 093002.

[43] J.I. Flege, E.E. Krasovskii, Intensity-voltage low-energy electron microscopy for functional materials characterization, Phys. Status Solidi Rapid Res. Lett. 8 (2014) 463–477.

[44] R.M. Tromp, J.B. Hannon, A.W. Ellis, W. Wan, A. Berghaus, O. Schaff, A new aberration-Corrected, energy-filtered LEEM/PEEM instrument. I, Princ. Des. Ultramicroscopy 110 (2010) 852–861.

[45] J.A. Venables, G.D.T. Spiller, M. Hanbücken, Nucleation and growth of thin films, Rep. Prog. Phys. 47 (1984) 399–459.

[46] J.I. Flege, P. Sutter, Nanoscale analysis of Ru(0001) oxidation using low-energy and photoemission electron microscopy, J. Phys. Condens. Matter 21 (2009) 314018.

[47] J.-F. Jerratsch, X. Shao, N. Nilius, H.-J. Freund, C. Popa, M.V. Ganduglia-Pirovano, A.M. Burow, J. Sauer, Electron localization in defective ceria films: a study with scanning-Tunneling microscopy and density-functional theory, Phys. Rev. Lett. 106 (2011) 246801.

[48] D.C. Grinter, R. Ithnin, C.L. Pang, G. Thornton, Defect structure of ultrathin ceria films on Pt(111): atomic views from scanning tunnelling microscopy, J. Phys. Chem. C 114 (2010) 17036–17041.

[49] C. Castellarin-Cudia, S. Surnev, G. Schneider, R. Podlicky, M.G. Ramsey, F.P. Netzer, Strain-Induced formation of arrays of catalytically active sites at the metal-oxide interface, Surf. Sci. 554 (2004) L120–L126.

[50] Y. Pan, N. Nilius, H.-J. Freund, J. Paier, C. Penschke, J. Sauer, Titration of Ce^{3+} ions in the $CeO_2(111)$ surface by Au adatoms, Phys. Rev. Lett. 111 (2013) 206101.

[51] S. Torbrügge, M. Reichling, A. Ishiyama, S. Morita, Ó. Custance, Evidence of subsurface oxygen vacancy ordering on reduced $CeO_2(111)$, Phys. Rev. Lett. 99 (2007) 56101.

[52] T. Hasegawa, S.M.F. Shahed, Y. Sainoo, A. Beniya, N. Isomura, Y. Watanabe, T. Komeda, Epitaxial growth of $CeO_2(111)$ Film on Ru(0001): scanning tunneling microscopy (STM) and X-Ray photoemission spectroscopy (XPS) study, J. Chem. Phys. 140 (2014) 044711.

[53] S. Fölsch, U. Barjenbruch, M. Henzler, Atomically thin epitaxial films of NaCl on germanium, Thin Solid Films 172 (1989) 123–132.

[54] C. Schwennicke, J. Schimmelpfennig, H. Pfnür, Morphology of thin NaCl films grown epitaxially on Ge(100), Surf. Sci. 293 (1993) 57–66.

[55] P.W. Sutter, J.-I. Flege, E.A. Sutter, Epitaxial graphene on ruthenium, Nat. Mater. 7 (2008) 406–411.

[56] E. Sutter, P. Albrecht, F.E. Camino, P. Sutter, Monolayer graphene as ultimate chemical passivation layer for arbitrarily shaped metal surfaces, Carbon 48 (2010) 4414–4420.

[57] E. Sutter, P. Albrecht, P. Sutter, Graphene growth on polycrystalline Ru thin films, Appl. Phys. Lett. 95 (2009) 133109.

[58] D.R. Mullins, S.H. Overbury, D.R. Huntley, Electron spectroscopy of single crystal and polycrystalline cerium oxide surfaces, Surf. Sci. 409 (1998) 307–319.

[59] M. Baron, O. Bondarchuk, D. Stacchiola, S. Shaikhutdinov, H.J. Freund, Interaction of gold with cerium oxide supports: $CeO_2(111)$ thin films vs CeO_x nanoparticles, J. Phys. Chem. C 113 (2009) 6042–6049.

[60] J.I. Flege, B. Kaemena, A. Meyer, J. Falta, S.D. Senanayake, J.T. Sadowski, R.D. Eithiraj, E.E. Krasovskii, Origin of chemical contrast in low-energy electron reflectivity of correlated multivalent oxides: the case of ceria, Phys. Rev. B 88 (2013) 235428.

[61] J. Höcker, T.O. Menteş, A. Sala, A. Locatelli, T. Schmidt, J. Falta, S.D. Senanayake, J.I. Flege, Unraveling the dynamic nanoscale reducibility ($Ce^{4+} \rightarrow Ce^{3+}$) of CeO_x-Ru in hydrogen activation, Adv. Mater. Interfaces (2015) 1500314.

[62] S. Alayoglu, K. An, G. Melaet, S. Chen, F. Bernardi, L.W. Wang, A.E. Lindeman, N. Musselwhite, J. Guo, Z. Liu, M.A. Marcus, G.A. Somorjai, Pt-Mediated reversible reduction and expansion of CeO_2 in Pt Nanoparticle/Mesoporous CeO_2 catalyst: tD:-In situ X-ray spectroscopy and diffraction studies under redox (H_2 and O_2) atmospheres, J. Phys. Chem. C 117 (2013) 26608–26616.

[63] C.L. Dong, A. Augustsson, C.L. Chen, C.L. Chang, Y.Y. Chen, J.H. Guo, Electronic structure and valence state of $CeAl_2$ from X-Ray absorption and emission spectroscopy, J. Electron Spectrosc. Relat. Phenom. 144-147 (2005) 581–584.

[64] H.-T. Chen, Y.M. Choi, M. Liu, M.C. Lin, A theoretical study of surface reduction mechanisms of $CeO_2(111)$ and (110) by H_2, ChemPhysChem 8 (2007) 849–855.

[65] D. Fernández-Torre, J. Carrasco, M.V. Ganduglia-Pirovano, R. Pérez, Hydrogen activation, diffusion, and clustering on $CeO_2(111)$: a DFT + U study, J. Chem. Phys. 141 (2014) 14703.

[66] M. García-Melchor, N. López, Homolytic products from heterolytic paths in H_2 dissociation on metal oxides: the example of CeO_2, J. Phys. Chem. C 118 (2014) 10921–10926.

[67] V. Stetsovych, F. Pagliuca, F. Dvořák, T. Duchoň, M. Vorokhta, M. Aulická, J. Lachnitt, S. Schernich, I. Matolínová, K. Veltruská, T. Skála, D. Mazur, J. Mysliveček, J. Libuda, V. Matolín, Epitaxial cubic Ce_2O_3 films via Ce-CeO_2 interfacial reaction, J. Phys. Chem. Lett. 4 (2013) 866–871.

[68] T. Duchoň, F. Dvořák, M. Aulická, V. Stetsovych, M. Vorokhta, D. Mazur, K. Veltruská, T. Skála, J. Mysliveček, I. Matolínová, V. Matolín, Ordered phases of reduced ceria as epitaxial films on Cu(111), J. Phys. Chem. C 118 (2014) 357–365.

[69] J.I. Flege, J. Hrbek, P. Sutter, Structural imaging of surface oxidation and oxidation catalysis on Ru(0001), Phys. Rev. B 78 (2008) 165407.

[70] J.I. Flege, J. Lachnitt, D. Mazur, P. Sutter, J. Falta, Role of $RuO_2(100)$ in surface oxidation and CO oxidation catalysis on Ru(0001), Phys. Chem. Chem. Phys. 18 (2016) 213–219.

[71] J.I. Flege, B. Herd, J. Goritzka, H. Over, E.E. Krasovskii, J. Falta, Nanoscale origin of mesoscale roughening: real-time tracking and identification of three distinct ruthenium oxide phases in ruthenium oxidation, ACS Nano (2015).

[72] E.E. Krasovskii, J. Höcker, J. Falta, J.I. Flege, Surface resonances in electron reflection from overlayers, J. Phys. Condens. Matter 27 (2015) 35501.